https://doi.org/10.1007/s41230-021-1124-5

Tailoring microstructure evolution and mechanical properties of a high-performance alloy steel through controlled thermal cycles of a direct laser depositing process

**Shi-yun Dong[1], **Xuan Zhao[1,2], Shi-xing Yan[1], Yao-hui Lü[1], Xiao-ting Liu[1], Yu-xin Liu[1], Peng He[2], Bin-shi Xu[1,2]

1. National Key Laboratory for Remanufacturing, Army Academy of Armored Forces, Beijing 100072, China

2. State Key Laboratory of Advanced Welding and Joining, Harbin Institute of Technology, Harbin 150001, China

Abstract: Direct laser deposition (DLD), as a popular metal additive manufacturing process, shows advantages of technical flexibility and high efficiency to gain a high-performance alloy steel component. However, during the processing of DLD, the deposited steel layer is affected by the subsequent layer depositing. The DLD block shows different microstructure and mechanical properties at the bottom, middle and top of the deposited parts. To date, there are few research works about the effects of inter-layer interval time and laser power on the microstructure evolution and mechanical properties of the deposited layers. In this study, the idle time and laser power layer by layer during DLD of 12CrNi2 steel were controlled to cause the deposited layers to maintain a high cooling rate, while the bottom deposited layer was subjected to a weak tempering effect. Results show that a high proportion of martensite is produced, which improves the strength of the deposited layer. Under the laser scanning strategy of laser power 2,500 W, scanning velocity 5 mm·s^{-1}, powder feeding rate 11 g·min^{-1}, overlap rate 50%, and a laser power difference of 50 W and a 2 min interval, the tensile strength of the deposited layer of 12CrNi2 steel is in the range of 873–1,022 MPa, and the elongation is in the range of 16.2%–18.9%. This study provides a method to reduce the tempering effect of the subsequent deposition layers on the bottom layers, which can increase the proportion of martensite in the low-alloy high-strength steel, so as to improve the yield strength of the alloy steel.

Key words: alloy steel; direct laser deposition; thermal cycles; microstructure evolution; mechanical properties

CLC numbers: TG142.33^{+}1 **Document code:** A **Article ID:** 1672-6421(2021)05-463-11

1 Introduction

As a typical and popular high-performance alloy steel, 12CrNi2 steel with high strength and high toughness can be used to manufacture the camshaft of a diesel engine for a nuclear power plant [1]. 12CrNi2 steel products are mainly fabricated via forging and heat treatment processes, which have the disadvantages of long processing period, complex procedures, high energy consumption, and low productive efficiency. Direct laser deposition (DLD), as a novel and advanced metal additive manufacturing technology, can realize near net-shape manufacturing of metal components [2-4]. DLD can directly prepare engineering components without additional tools by creating continuous cross-section layers from 3D scanning system data [5]. In the DLD process, metal powders are melted, solidified and cooled rapidly to form a cladding layer on the substrate surface. Engineering parts made by DLD show an ultra-fine microstructure and excellent mechanical properties [6].

Some research works studied the microstructure evolution and mechanical properties of low alloy steel prepared with different DLD processing parameters. Zhou et al. [7] and Guan et al. [8] focused on the effects of laser power or laser incident energy on microstructure

***Shi-yun Dong**

Ph.D., Professor. His research interests mainly focus on surface engineering, laser additive manufacturing and remanufacturing technology of high performance metal materials. He successfully fabricated the large-scale and complex structured high performance alloy steel pieces by selective laser melting processing, remanufactured high strength steel components such as gears and impellers via laser additive processing, and restored the worn blades with nanoparticle reinforced composite coatings. He has published over 100 SCI/EI indexed papers, and possesses 20 invention patents of China.

E-mail: syd422@sohu.com

****Xuan Zhao**

E-mail: zhaoxedu@163.com

Received: 2021-07-25; Accepted: 2021-09-21

evolution and mechanical behavior of DLD low alloy steel. It was found that laser incident energy has a significant effect on the morphology of bainite. Dong et al. [9] studied the effect of oxygen content in powders on the microstructure and mechanical properties of DLD 12CrNi2 low alloy steel. This study demonstrated that porosity occurred when high oxygen alloy powders were used in the DLD process. Zuo et al. [10] found that the microstructure evolution, heating behavior or temperature field of 24CrNiMoY low alloy steel were significantly affected by the scanning speed during DLD.

The cooling time between two deposited layers plays a key role on microstructure and mechanical properties. Zheng et al.[11] used the alternating direction explicit finite difference method to numerically study the thermal behavior of the deposited layers during DLD process. The results showed that the temperature at the end of each layer increased with the shortening of time interval. Costa et al. [12] studied the effect of interlayer time interval on the microstructure and hardness of AISI 420 alloy steel. They found that increasing the inter-layer time interval decreased the average temperature of DLD AISI 420 steels. Manvatkar et al. [13] found that the cooling rate significantly decreased and the layer peak temperature significantly increased from the first layer to the fifth layer during DLD process. Yadollahi et al. [14] found a longer interlayer time interval increased the cooling rate of each layer, resulted in a finer microstructure and higher tensile strength of DLD 316L stainless steel. These studies show that the thermal behavior of DLD metal layers depends greatly on the heat transfer conditions during the DLD process. Compared with the longer time interval, a shorter time interval can reduce heat consumption, slow down the heat transfer loss and help to reduce the cooling rate of the upper layer. This reduces the ratio of austenite to martensite and the strength of DLD parts. Kang et al. [15] found that in the DLD process of high strength low alloy steel, the bottom layers were tempered by the subsequent deposition layers, which caused the bottom layers to present a tempered microstructure, and the yield strength was decreased.

In this study, three scanning strategies were designed for DLD process to analyze the thermal behavior, microstructure, and mechanical properties of the deposited 12CrNi2 steel blocks. The temperature cycling characteristics were changed through scanning strategy to maintain a higher cooling rate and a weaker tempering effect of the deposited layer, and to increase the martensite (M) structure proportion in the deposited layer, so as to improve the comprehensive tensile properties of the DLD 12CrNi2 steel.

2 Experimental procedure

The powder materials used for DLD were prepared via vacuum induction melting and gas-atomization under argon protection. The chemical composition of the powders is designed according to the National Standard of China (GB/T 3077-2015) as follows (in wt.%): 0.12 C, 1.59 Ni, 1.00 Cr, 0.57 Mn, 0.34 Si, 0.008 O, with balance Fe, i.e., the chemical composition of 12CrNi2 alloy steel. Figure 1 shows the powder particle morphology and particle size distribution. The powder particle size ranges from 80 μm to 222 μm, with a mean size of 136 μm. Before DLD, the powders were dried for 2 h at 120 °C in a vacuum drying oven. The size of the deposited layers is about 50 mm×20 mm×8 mm. Q235 steel plates with dimensions of 210 mm×190 mm×15 mm were used as deposition substrates, with the nominal composition in wt.%: C ≤ 0.22, Si ≤ 0.35, Mn ≤ 1.40, S ≤ 0.050, P ≤0.045, and balance Fe.

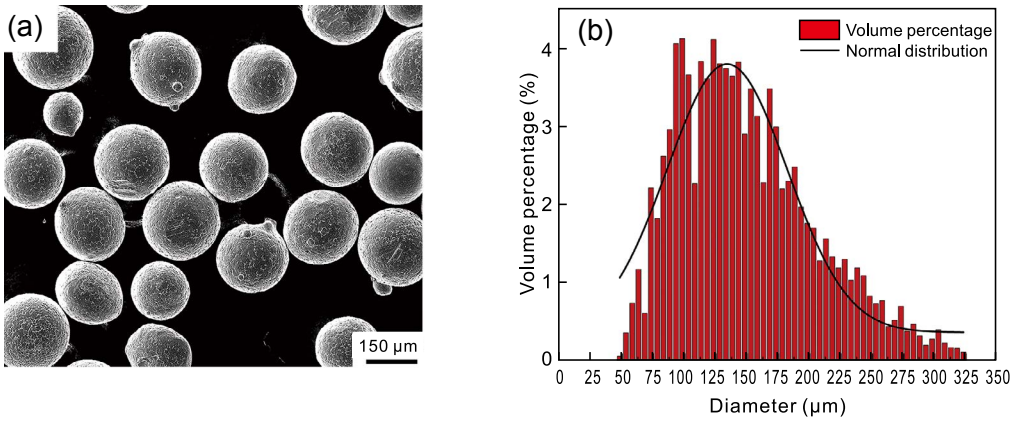

Fig. 1: SEM morphology (a) and size distribution (b) of powder particles

The DLD experiments were carried out using a DLD system (a maximum output power of 3,000 W and a spot diameter of 3 mm) with a computer control 6-axis robot, a powder delivery nozzle equipped with an argon shield apparatus, and a computer system as shown in Fig. 2. The processing parameters of DLD process adopted in the experiments were: laser power 2,500 W, scanning velocity 5 mm·s^{-1}, powder feeding rate 11 g·min^{-1}, and overlap rate 50%. The thickness of each layer of the DLD was about 1.0 mm. The reciprocating scanning strategy was used during the deposition process. Three scanning strategies were designed as follows: Strategy 1 (S1) constituted successive deposition without any time interval between individual layers. Strategy 2 (S2) included an interval of 2 min between successive layers. Meanwhile, in Strategy 3 (S3), a laser power difference of 50 W and a 2 min interval were included between successive

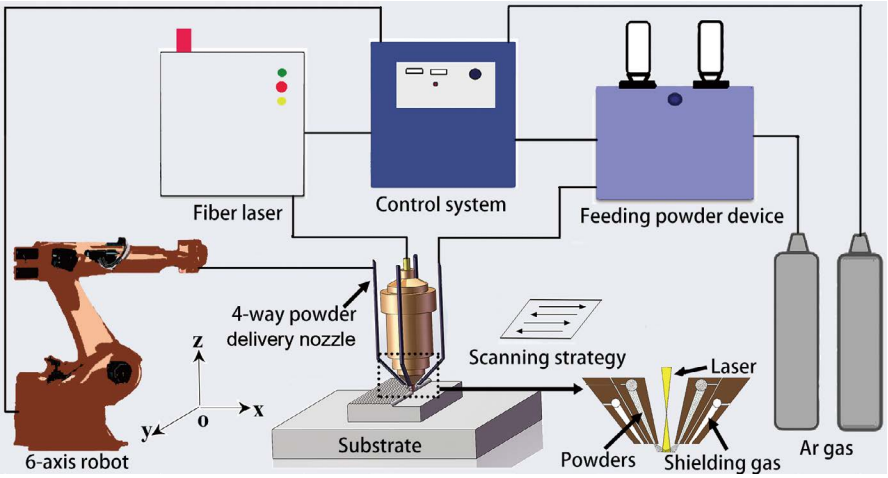

Fig. 2: Schematic diagram of direct laser deposition (DLD) system

deposited layers. The samples fabricated using the scanning Strategies S1, S2, and S3 were denoted as Samples S1, S2, and S3, respectively.

The DLD samples were sectioned apart from the substrate via a spark erosion wire cutting machine. The samples were ground and polished, and then etched with an alcohol nitrate solution (5 mL HNO_3 + 95 mL C_2H_5OH) for microstructure characterization. Microstructures were characterized using a field emission scanning electron microscope. The tensile samples, as shown in Fig. 3, were cut along the scanning direction. The tensile tests were carried out at room temperature with a loading speed of 0.5 mm·min^{-1}. Vickers hardness was measured under the load of 2.945 N with the load-dwelling time of 15 s.

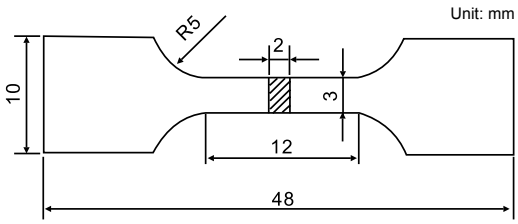

Fig. 3: Dimensions of tensile samples at room temperature

3 Results and discussion

3.1 Thermal cycles

3.1.1 Thermal cycle curves

Thermal cycling during DLD in different regions of the steel sample was simulated using the finite-element method (Abaqus 2017). Figure 4 shows the thermal cycle curves of the DLD process using the three scanning strategies. The curves in different colors represent the deposition layer of different heights. It can be seen from Fig. 4(a) with S1 scanning strategy, the highest temperatures inside the molten pool of the first, third and fifth deposited layers are 2677.3 °C, 3113.3 °C and 3269.7 °C, respectively. In addition, when the first layer, the third layer, and the fifth layer are deposited by laser melting, the initial temperatures of the deposited layers are 25 °C, 184 °C, and 251.9 °C, respectively. When the first deposition layer is prepared, the good heat transfer conditions of the substrate cause a low heat accumulation of the deposition layer. With the increase in the number of deposited layers, the heat transfer conditions of the deposited layers become worse, so that the heat accumulation of the subsequent deposited layers increases, which in turn leads to a significant increase in the maximum temperature inside the molten pool. So, the continuous deposition scanning strategy will generate significant heat accumulation inside the deposition layer. Therefore, a scanning Strategy 2 with cooling for 2 min between deposition layers was designed to improve the heat transfer conditions during the melting and deposition process. Figure 4(b) shows the thermal cycle curves of the 12CrNi2 alloy steel with scanning Strategy 2. The highest temperatures inside the molten pool of the first, third and fifth layers are 2677.3 °C, 2883.9 °C and 2988.3 °C, and the initial temperatures of the deposited layer are 25 °C, 60.6 °C and 98.5 °C, respectively. Extending the cooling time between the deposited layers improves the heat transfer conditions of the deposited layers, thereby effectively reducing the heat accumulation of the subsequent deposited layers and the maximum temperature inside the molten pool. However, cooling for 2 min between the deposition layers failed to completely avoid the accumulation of heat inside the deposition layer, and the highest temperature inside the molten pool of the third and fifth deposition layers was still higher than that of the first layer. To further reduce the heat accumulation in the deposited layer during the melting and deposition process, a scanning Strategy 3 of cooling between the deposited layers for 2 min + laser power decreasing by 50 W layer by layer was designed. Figure 4(c) shows the thermal cycle curve when preparing 12CrNi2 alloy steel using scanning Strategy 3. The highest temperatures inside the molten pool of the first, third and fifth layers are 2677.3 °C, 2394.8 °C and 2063.7 °C, and the initial temperatures of the deposited layers are 25 °C, 58.4 °C and 88.9 °C, respectively. For Strategy 3, as the number of deposited layers increases, the maximum temperature inside the deposited layer molten pool shows a gradual decrease. The different temperature gradient distribution in the molten pool not only affects the

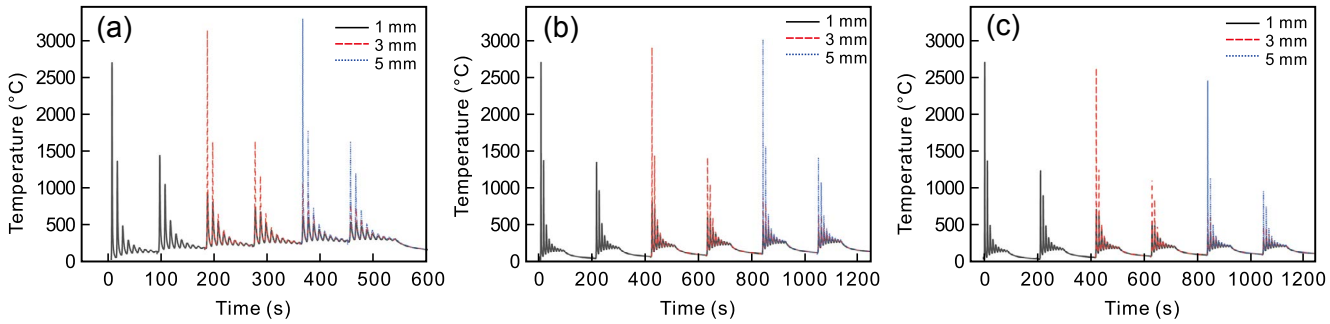

Fig. 4: Thermal cycle curves under different scanning strategies during DLD: (a) S1; (b) S2; (c) S3

solidification structure of the deposited layer, but also has different tempering effects on the deposited layer. Therefore, the evolution of the deposited alloy steel structure under different scanning strategies was further analyzed based on the above temperature field finite element simulation results.

3.1.2 Variation of cooling rates

The study by Kang et al. [16] showed that the cooling rate of the deposited layer from the A_3 temperature to the M_S temperature during the continuous cooling process would determine the room temperature structure of the deposited alloy steel. Therefore, this section will analyze the cooling rate change law of the deposited layer from the A_3 temperature to the M_S temperature range under different scanning strategies based on the finite element simulation results of the temperature field, and provide a reference for the study of the structure evolution law of laser melting deposited alloy steel. Figure 5(a) shows the changing law of the cooling rate of the deposited layer of alloy steel prepared under the continuous deposition strategy (Strategy 1). It can be seen from Fig. 5(a) that the cooling rate of the first pass of the first layer of the 12CrNi2 alloy steel deposition layer prepared by Strategy 1 is 761.2 °C·s^{-1}. During the laser melting and deposition process, the substrate is continuously heated to increase the heat accumulation, which reduces the cooling rate of the 9th pass of the first layer to 417.5 °C·s^{-1}. With an increase in the number of deposited layers, the increase in heat accumulation results in the average cooling rates of the second to sixth deposited layers decreasing to 328.5, 254.7, 201.9, 160.4 and 143.8 °C·s^{-1}, respectively. It can be calculated from the data in Fig. 5(b) that the average cooling rates of the first to the sixth layers of the 12CrNi2 alloy steel prepared by Strategy 2 are 514.0, 408.9, 350.1, 289.4, 250.4 and 232.2 °C·s^{-1}, respectively. Comparing with Strategy 1, samples by Strategy 2 have a higher average cooling rate for the second to sixth layers of the 12CrNi2 alloy steel. This is because Strategy 2 has lower heat accumulation, which makes the heat transfer speed of the deposited layer faster. Therefore, as the number of deposited layers increases, the average cooling rate of the deposited layer prepared by scanning Strategy 2 will be higher than that of scanning Strategy 1. Figure 5(c) shows the cooling rate change curve of the deposition layer prepared by Strategy 3 with an interval of 2 min between the deposition layers and the laser power decreasing 50 W layer by layer. The average cooling rates of the first to the sixth layers are 503.5, 451.1, 433.2, 424.1, 433.1 and 448.8 °C·s^{-1}, respectively, which are higher than that of Strategy 2. Strategy 3 reduces the degree of overheating inside the molten pool of the deposited layer and enables the deposited layer to obtain a higher cooling rate. As mentioned above, the proportion of M structure in the alloy steel obtained after continuous cooling transformation increases with the increase of the cooling rate. Therefore, it can be inferred that the M structure ratio of the deposited alloy steel prepared by scanning Strategy 3 will be higher than Strategy 1 and Strategy 2.

3.1.3 Intrinsic heat treatment

During the laser melting deposition process, the deposited layer is tempered by the subsequent deposited layer, and then a tempered structure is generated inside the deposited layer (a tempered structure generally consists of precipitated phases and tempered matrix). Therefore, in addition to the cooling rate, the tempering temperature and time of the deposited layer of alloy steel also significantly affects the room temperature structure characteristics of the deposited layer. The temperature field data

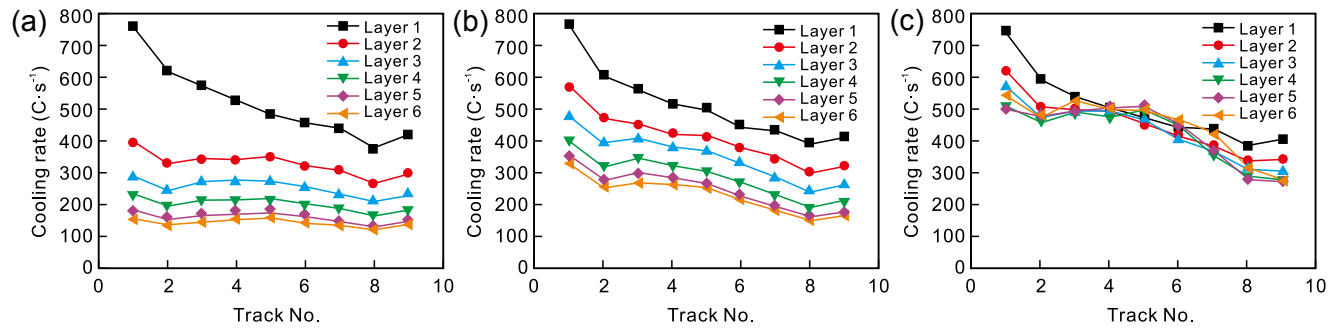

Fig. 5: Cooling rate of deposited layers under different scanning strategies during DLD: (a) S1; (b) S2; (c) S3

at three points located in the bottom (1 mm high), middle (3 mm high), and top region (5 mm high) of the deposited sample were extracted and used to analyze the tempering temperature-time variation law of the deposited alloy steel. Figure 6(a) shows the tempering time at different temperatures of different regions of the alloy steel deposition layer prepared by scanning Strategy 1. The residence times of the bottom region of the deposition layer in the range of 250–400 °C, 401–600 °C and 601–750 °C are 256 s, 89.1 s and 18.9 s, respectively. When the tempering temperature is in the range of 250–400 °C, the supersaturated carbon atoms in the α-phase gradually separate out, and then the carbide precipitation is formed, which is generally θ-carbide (Fe_3C). At this time, the α-phase still maintains the deposited block or lath morphology. When the tempering temperature reaches 401–600 °C, the precipitated carbides gradually aggregate and spheroidize, and finally form granular cementite or carbon-rich structure (M-A islands). Then, the α-phase begins to recover to a certain extent, and the lath boundary of the α-phase gradually becomes blurred. When the tempering temperature is higher than 600 °C, the spheroidized carbides further aggregate and grow, forming a larger-sized granular cementite or carbon-rich structure (M-A island element). In this case, the α-phase will recrystallize, and the lath structure will gradually be replaced by the equiaxed structure with very low dislocation density. Since the bottom region deposited by scanning Strategy 1 is subjected to a short tempering time, the structure in this area will have both the characteristics of the deposited state and the tempered state. The residence times of the middle region of the deposition sample at 250–400 °C, 401–600 °C and 601–750 °C are 224 s, 79.5 s and 24.4 s, respectively, and 110.5 s, 62.3 s and 8.9 s, respectively for the top region. It can be seen that the tempering time of the bottom region is the longest, followed by the middle region, and the top region is the shortest. Figure 6(b) is a histogram of the tempering temperature-time of the alloy steel deposition layer prepared by Strategy 2. The residence times of the bottom region at 250–400 °C, 401–600 °C and 601–750 °C are 187.8 s, 37.7 s and 6.2 s, respectively; that of the middle region are 171.6 s, 36 s and 7.5 s; and of the top region are 125 s, 22.7 s and 5 s, respectively. The heat accumulation inside the deposited sample prepared by Strategy 2 is significantly lower than that of Strategy 1, which makes the heat transfer speed between the substrate and the deposited layer faster. Therefore, the residence time in the temperature range of 250–750 °C is significantly shortened. Figures 6(c) shows the tempering temperature-time change of the alloy steel deposited by scanning Strategy 3. The residence times of the bottom region of the sample at 250–400 °C, 401–600 °C and 601–750 °C are 61 s, 20.1 s and 3.2 s, respectively; that of the middle region are 54.5 s, 18.3 s, and 3.7 s; and of the top region are 33.2 s, 9.3 s, and 2 s, respectively. As mentioned above, compared with scanning Strategy 2, the maximum temperature inside the molten pool and the heat accumulation of the deposited layer formed with Strategy 3 are lower, which increases the heat transfer rate of the deposited layer. Therefore, the residence time of the deposited layer prepared by scanning Strategy 3 in the above temperature range is lower than that of Strategy 2.

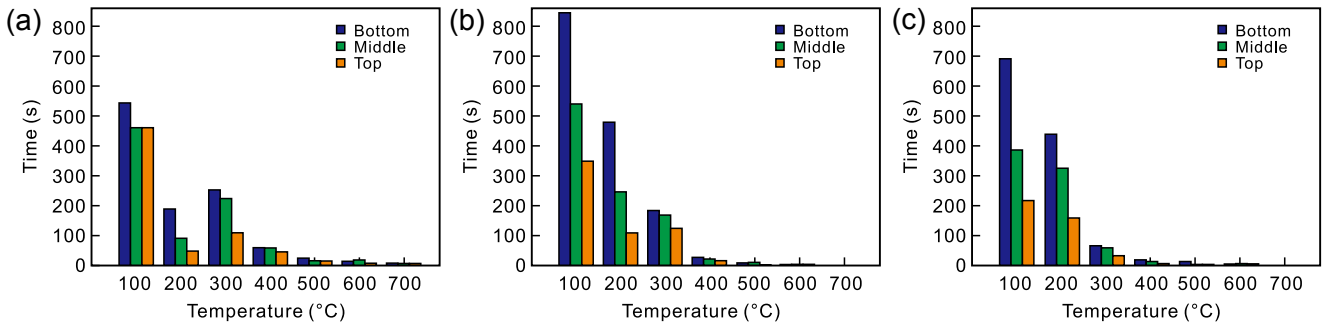

Fig. 6: Tempering temperature-time of deposited layers under different scanning strategies during DLD: (a) Strategy 1; (b) Strategy 2; (c) Strategy 3

In summary, the residence time of the same area in the deposition layer prepared by the three scanning strategies is different in a certain temperature range. The three scanning strategies in descending order of residence time are Strategy 1, Strategy 2, and Strategy 3. Under the same scanning strategy, and in a certain temperature range, the different areas of the deposition layer arranged in descending order of residence time is: bottom, middle and top area. Due to different tempering times, the α-phase matrix and carbide precipitation of the deposited layer have different microstructure evolution laws. Meanwhile, different tempering temperature-time conditions can produce different degrees of desolventizing in the martensite and bainite structure inside the deposited layer, thereby affecting the mechanical properties of the alloy steel deposited layer. Therefore, the tempering temperature-time data can be used to analyze the microstructure evolution process and mechanical properties of different areas of the alloy steel deposition layer.

3.2 Microstructure evolution

3.2.1 Continue cooling transformation

During the laser melting deposition process, the alloy steel powder quickly melts and solidifies to form an alloy steel deposition layer. During the solidification and cooling from liquid state to room temperature, a variety of structural transformations within the deposition layer overlap each other,

so that the alloy steel deposition layer obtains an uneven mixed structure. The continuous cooling transformation curve of undercooled austenite (referred to as the CCT diagram) reflects the microstructure evolution of undercooled austenite under continuous cooling conditions, and is an important basis for analyzing the structure and properties of alloy steel transformation products. The CCT diagram of 12CrNi2 alloy steel is shown in Fig. 7, which contains four continuous cooling curves of 0.1, 1, 10 and 100 °C·s^{-1}. These curves start from the austenite transformation start temperature (A_3) and end at the martensite transformation start temperature (M_S). The CCT diagram of 12CrNi2 alloy steel includes the proeutectoid ferrite (PF) transformation zone, the pearlite (P) transformation zone, the bainite (B) transformation zone and the martensite (M) transformation zone. As the cooling rate increases from 0.1 °C·s^{-1} to 100 °C·s^{-1}, the residence time of the cooling curve in the PF, P and B transformation zone is reduced, so that more subcooled austenite is retained at M_S. The M transition occurs below M_S. Therefore, as the cooling rate of the deposited layer increases, content of PF, P, and B in the deposited 12CrNi2 alloy steel decreases, and the proportion of M increases.

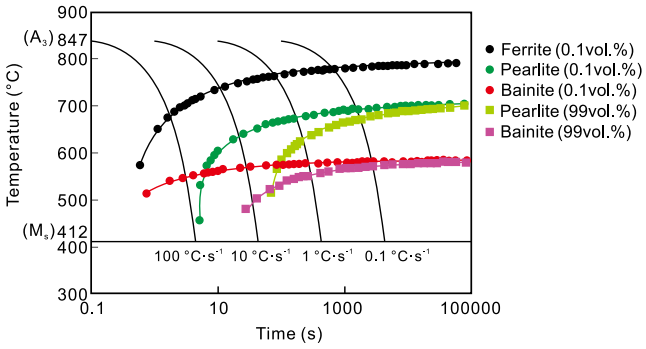

Fig. 7: CCT diagram of 12CrNi2 alloy steel

3.2.2 Grain structure

Figure 8 shows the grain size distribution of 12CrNi2 alloy steel prepared under different scanning strategies. The average grain sizes of the top, middle, and bottom regions of the S1 sample are 9.7 μm^2 [Fig. 8(a)], 9.4 μm^2 [Fig. 8(d)] and 12 μm^2 [Fig. 8(g)], respectively. It can be seen from the analysis in Section 3.1.3 that the bottom region of the S1 sample is subjected to the subsequent tempering of the deposition layers for a long time, and the residence time in the temperature range of 601–750 °C is 18.9 s. The tempering effect of the S1 sample will cause the recrystallization behavior of its bottom region, so that the grain size in the bottom region is greater than that in the middle and top

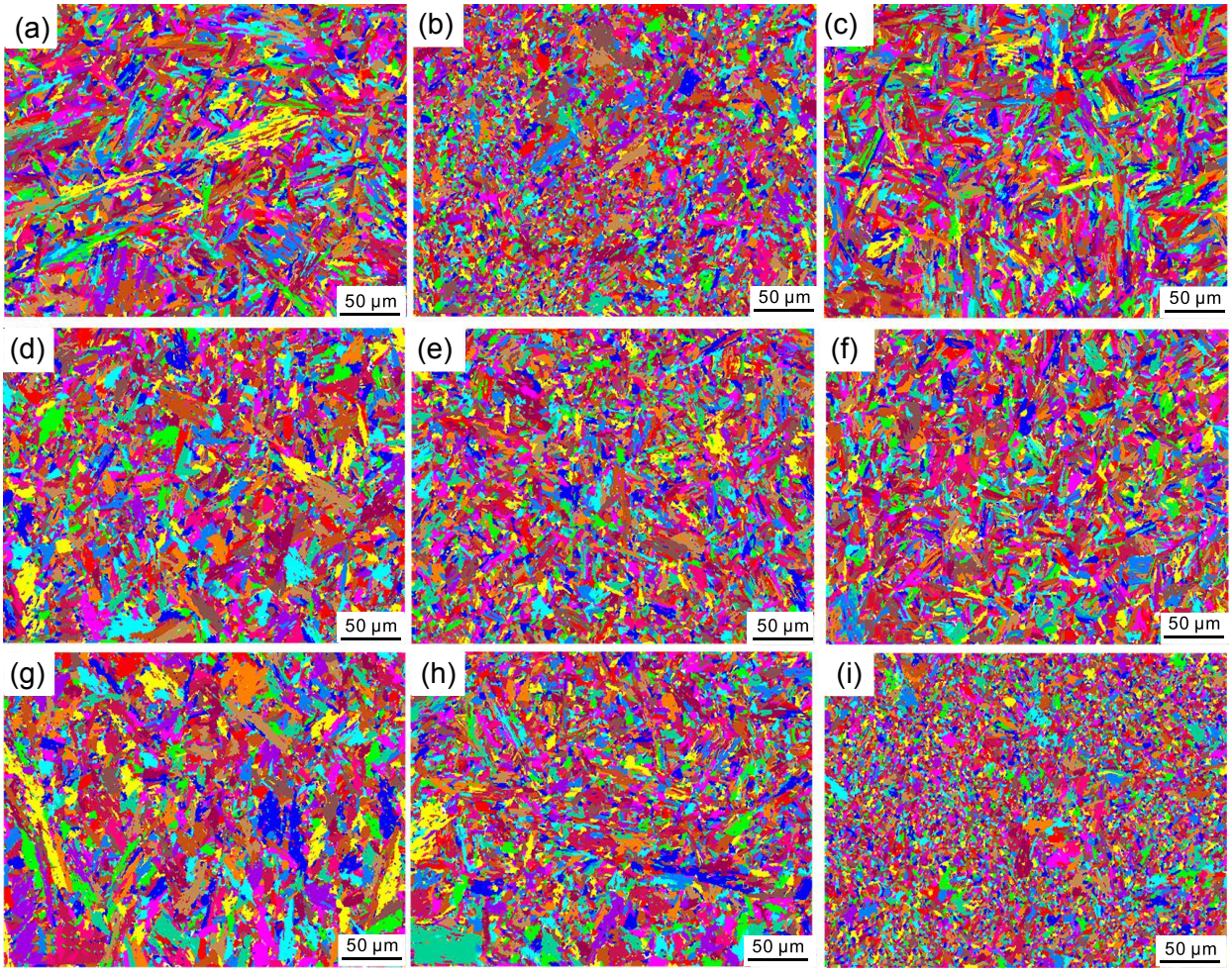

Fig. 8: Unique grain-colour map. Top region in samples S1 (a), S2 (b), and S3 (c); middle region in samples S1 (d), S2 (e), and S3 (f); bottom region in samples S1 (g), S2 (h), and S3 (i)

regions. The grain sizes of the top, middle and bottom regions of the S2 sample are 6.8 μm^2 [Fig. 8(b)], 7.3 μm^2 [Fig. 8(e)] and 8.7 μm^2 [Fig. 8(h)], respectively. The middle and bottom regions of the S2 sample are tempered by the subsequent deposition sample, and the residence time at 601–750 °C is 6.2 s, which causes the middle and bottom region of the deposition sample to regenerate to a certain extent. The average grain sizes of the top, middle, and bottom of the S3 sample are 8.9 μm^2 [Fig. 8(c)], 7.4 μm^2 [Fig. 8(f)], and 4.9 μm^2 [Fig. 8(i)], respectively. It can be seen that the bottom and middle region of the S3 sample are minorly affected by the subsequent deposition layers, and the residence time at 601–750 °C is about 3.2 s. Therefore, there is no obvious abnormal growth of crystal grains in the middle and bottom regions of the S3 sample.

Figure 9 shows the statistical graph of grain size of the DLD 12CrNi2 alloy steel, where the percentages of grain size below 10 μm^2 in the top, middle and bottom regions of the S1 sample [Fig. 9(a)] are 60%, 64%, and 50%, while that of the S2 sample [Fig. 9(b)] are 81%, 76%, and 68%, respectively. This is due to the 2 min interval between layers which reduces the heat accumulation of the deposited layer of the S2 sample, thereby increasing the nucleation rate during the solidification process and shortening the grain growth time, causing the number of grains below 10 μm^2 in the S2 sample to significantly increase. The percentage of grains with a size below 10 μm^2 in the top, middle and bottom regions of the S3 sample are 64%, 77% and 91%, respectively [Fig. 9(c)]. Compared with the S1 and S2 samples, S3 sample fabrication draws the lowest laser incident energy, and it has a lower heat accumulation, which further increases the nucleation rate of the crystal grains during the solidification process and reduces the nucleation time. The average percentage of grains with a size below 10 μm^2 in three regions of S1 sample, S2 sample and S3 sample are 58%, 75% and 77%, respectively. Therefore, the number of grains below 10 μm^2 in the S3 sample is further increased.

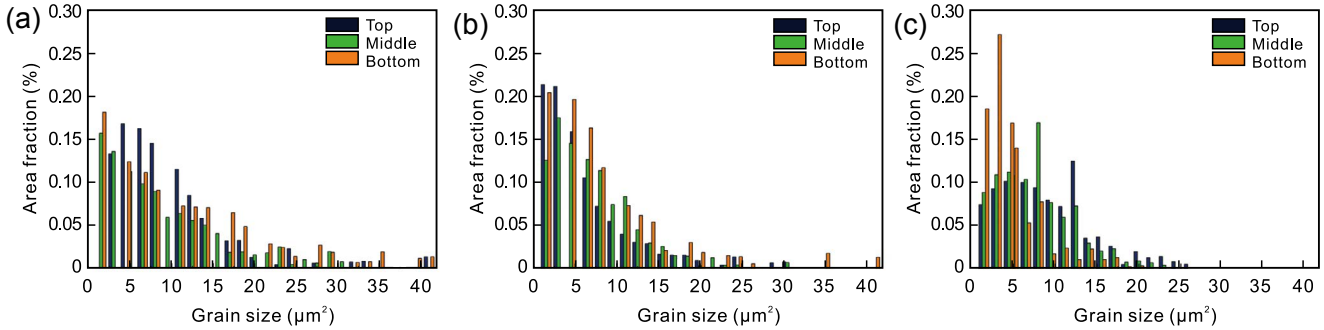

Fig. 9: Statistical graph of grain size of DLD 12CrNi2 alloy steel: (a) Sample S1; (b) Sample S2; (c) Sample S3

3.2.3 Solid-state phase transformation

The XRD diffraction patterns of laser melting deposited 12CrNi2 alloy steel are shown in Fig. 10. It can be seen from the figure that the five strong diffraction peaks correspond to the (110), (200), (211), (220) and (310) crystal planes of α-Fe. Compared with the standard card (PDF-06-0696, CAS#: 7439-89-6) of the powder diffraction file of α-Fe, the positions of 2θ in the XRD diffraction curve of the deposited 12CrNi2 alloy steel are offset. During the laser melting deposition process, the molten pools rapidly solidify to form a deposition layer, which causes most of the alloying element atoms in the α-Fe matrix to have insufficient time to diffuse, causing the lattice distortion of α-Fe matrix. Therefore, the diffraction peak position of the deposited 12CrNi2 alloy steel is shifted. So, the matrix phase of the as-deposited 12CrNi2 alloy steel can be expressed as α-Fe (M), where M represents alloying elements such as C, Cr, and Ni dissolved in the α-Fe matrix. Since the volume percentage of retained austenite and carbides in the deposited 12CrNi2 alloy steel is less than 5%, these phases have no obvious diffraction peaks on the XRD diffraction curves.

The SEM morphologies of the top, middle and bottom regions of Sample S1 are shown in Figs. 11(a), (d) and (g), respectively. The size of the network-like proeutectoid ferrite (PF_N) at the top of S1 sample is larger than in the middle and bottom regions. Inside the PF_N, there are islands of bainite ferrite (F_B) and martensite-austenite (M-A). It can be seen

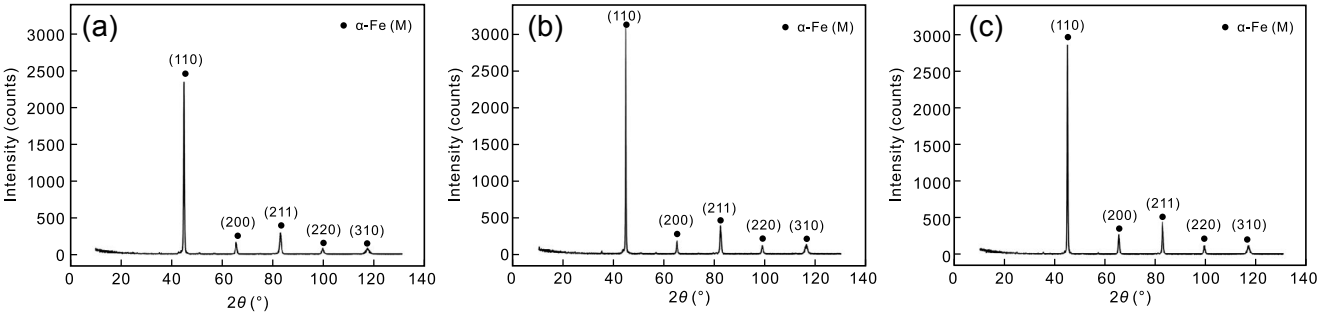

Fig. 10: XRD patterns of DLD 12CrNi2 alloy steel sample: (a) S1; (b) S2; and (c) S3

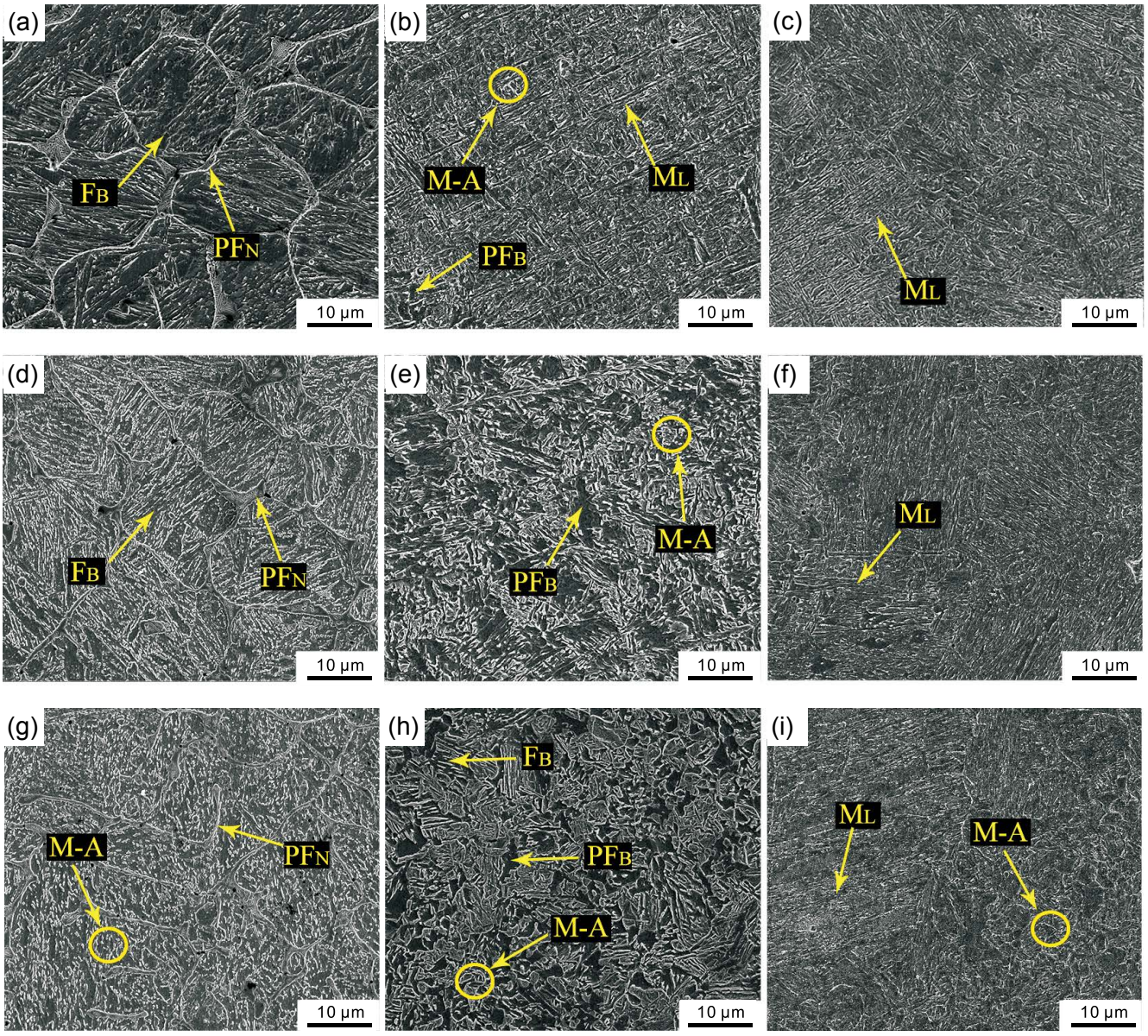

Fig. 11: SEM morphologies of DLD 12CrNi2 samples: (a) top, (d) middle, and (g) bottom layers in Sample 1; (b) top, (e) middle, and (h) bottom layers in Sample 2; (c) top, (f) middle, and (i) bottom layers in Sample 3

from Fig. 11(a) that the F_B at the top of the S1 sample presents lath morphology. The microstructure composed of PF_N and F_B is called Widmanstatite (W) structure. SEM morphologies of the top, middle and bottom of the S2 sample are shown in Figs. 11(b), (e) and (h). It can be seen that the S2 sample is mainly composed of lath martensite (M_L), PF_B and M-A islands. The top region of the S2 sample is mainly composed of M_L and M-A islands. M_L is formed by 12CrNi2 alloy steel rapidly cooled to below the M_S temperature. The M-A islands are composed of carbide, retained austenite and martensite. The middle region of the S2 sample is mainly composed of F_B, PF_B and M-A islands. Because the middle region is subjected to the tempering effect of subsequent deposited layers, the lath characteristics of F_B are no longer obvious. In addition, the number of PF_B and M-A islands in the middle region of the S2 sample is greater than in the top region. The bottom region of the S2 sample is also composed of F_B, PF_B and M-A island. Compared with the top and middle regions of the S2 sample, the bottom region is subject to the most times of tempering by subsequent depositions, resulting in a higher number of M-A islands in the bottom area than in the middle and top areas. The top region of the S3 sample is mainly composed of M_L. The number of M-A islands in this area is lower than that of S1 and S2 samples. The middle and bottom regions of the S3 sample are also mainly composed of M_L and M-A islands, and the number of M-A islands distributed on the M_L is lower than in the S1 and S2 samples.

3.3 Mechanical properties

3.3.1 Tensile properties

Figure 12 shows the engineering stress-strain curve of DLD alloy steel, and the data is listed in Table 1. As shown in Fig. 12(a), the maximum tensile strength (UTS) of the top, middle and bottom regions of the S1 sample is 1360 MPa,

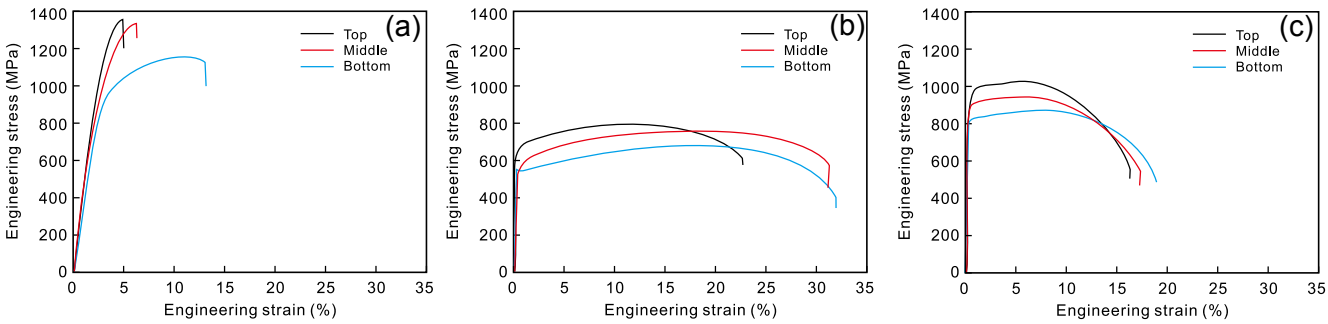

Fig. 12: Typical tensile stress-strain curves of DLD 12CrNi2 samples: (a) S1, (b) S2, and (c) S3

Table 1: Room-temperature tensile properties of DLD 12CrNi2 alloy steels

Samples	Position	UTS (MPa)	YS (MPa)	EL (%)
S1	Top	1360 ± 47	1019 ± 34	4.8 ± 1.6
	Middle	1337 ± 25	951 ± 16	6.3 ± 0.9
	Bottom	1154 ± 31	848 ± 43	13 ± 1.8
S2	Top	790 ± 19	563 ± 27	22.8 ± 0.7
	Middle	753 ± 33	480 ± 14	31.3 ± 2.1
	Bottom	672 ± 51	455 ± 20	31.9 ± 2.5
S3	Top	1022 ± 43	887 ± 22	16.2 ± 0.9
	Middle	942 ± 34	836 ± 26	17.3 ± 1.4
	Bottom	873 ± 13	751 ± 35	18.9 ± 2.0

1337 MPa and 1154 MPa, respectively. The elongation (EL) of the top, middle, and bottom regions of the sample is 4.8%, 6.3%, and 13%, respectively. The study by Karmakar et al. [17] shows that the internal microstructure of alloy steel prepared by DLD significantly affects its mechanical properties. The S1 sample in the top is mainly composed of Widmanstatten, and the plastic deformation ability of Widmanstatten is low, resulting in the high strength and low EL of S1 sample. As the number of deposited layers increases, the UTS shows a trend of increase and EL decreases. The middle and bottom regions of the S1 sample are composed of tempered W with higher deformability, which increases the EL in the middle and bottom region of the S1 sample. As shown in Fig. 12(b), the UTS of the top, middle and bottom region of the S2 sample is 790, 753 and 672 MPa, and the EL is 22.8%, 31.3%, and 31.9%, respectively. Under tensile loading, F_B and M_L in S2 sample have good plastic deformation ability, resulting in higher EL of S2 sample than S1 sample. In addition, the EL in the middle and bottom region of the S2 sample is higher than the top region due to the relatively lower proportion of M_L in the middle and bottom region. As shown in Fig. 12(c), the UTS of the top, middle and bottom region of the S3 sample is 1022, 942 and 873 MPa, and the EL is 16.2%, 17.3%, and 18.9%, respectively. The scanning strategy with idle time between layers and decreasing laser power layer by layer for S3 sample can decrease the inter-layer temperature and the top temperature of the molten pool, so that the deposition sample maintains a higher cooling rate and is subjected to a weaker tempering effect. The M_L number of the S3 sample is higher than that of the S2 sample. Therefore, the strength of the S3 sample is higher, but the EL is lower than that of the S2 sample.

Figure 13 shows the SEM fracture morphologies of the samples. As shown in Figs. 13(a), (d) and (g), the fracture surface at the top of the S1 specimen mainly includes cleavage surface and tearing edge, showing the feature of cleavage fracture. This region is mainly composed of brittle W, which makes it impossible to relieve stress concentration through plastic deformation. As the tensile load increases, the alloy steel material undergoes cleavage fracture. Compared with the top of the S1 sample, the number of tearing edges in the fracture surface of the middle part is increased. This is because the W structure in the middle of the S1 sample is tempered by the subsequent deposited layer, which improves the W deformability. Under tensile loading, the crack propagation path in the middle of the S1 specimen is more complicated, and then a tearing edge appears at the tensile fracture. The fracture surface of the bottom region of the S1 sample mainly includes tearing edges, dimples and a small amount of cleavage surfaces. Compared with the top and middle parts of the S1 sample, the in-situ tempering time of this part is longer, which improves the deformability of tempered W. Therefore, dimples appear on the tensile fracture surface at the bottom of the S1 sample. The SEM morphologies of the tensile fractures at the top, middle and bottom region of the S2 sample are shown in Figs. 13(b), (e) and (h). The tensile fracture morphology of the S2 sample includes dimples and cleavage surfaces, which are characterized by ductile fracture. The S2 sample is mainly composed of F_B, M_L and M-A islands. When a tensile load is applied, F_B and M_L in the S2 sample can reduce stress concentration through plastic deformation. As the tensile load increases, the pores gathered in the plastic deformation zone form dimples on the fracture surface. As shown in Figs. 13(c), (f) and (i), the cleavage fracture characteristics of the tensile fracture morphologies in the S3 sample are more obvious than in the S2 sample, which can explain that the EL of the S3 sample is lower than that of the S2 sample (see Table 1).

3.3.2 Hardness

The Vickers hardness curve of DLD alloy steel is shown in Fig. 14. The average hardnesses of the S1, S2 and S3 samples are 407 HV, 299 HV and 331 HV, respectively. The S1 sample is

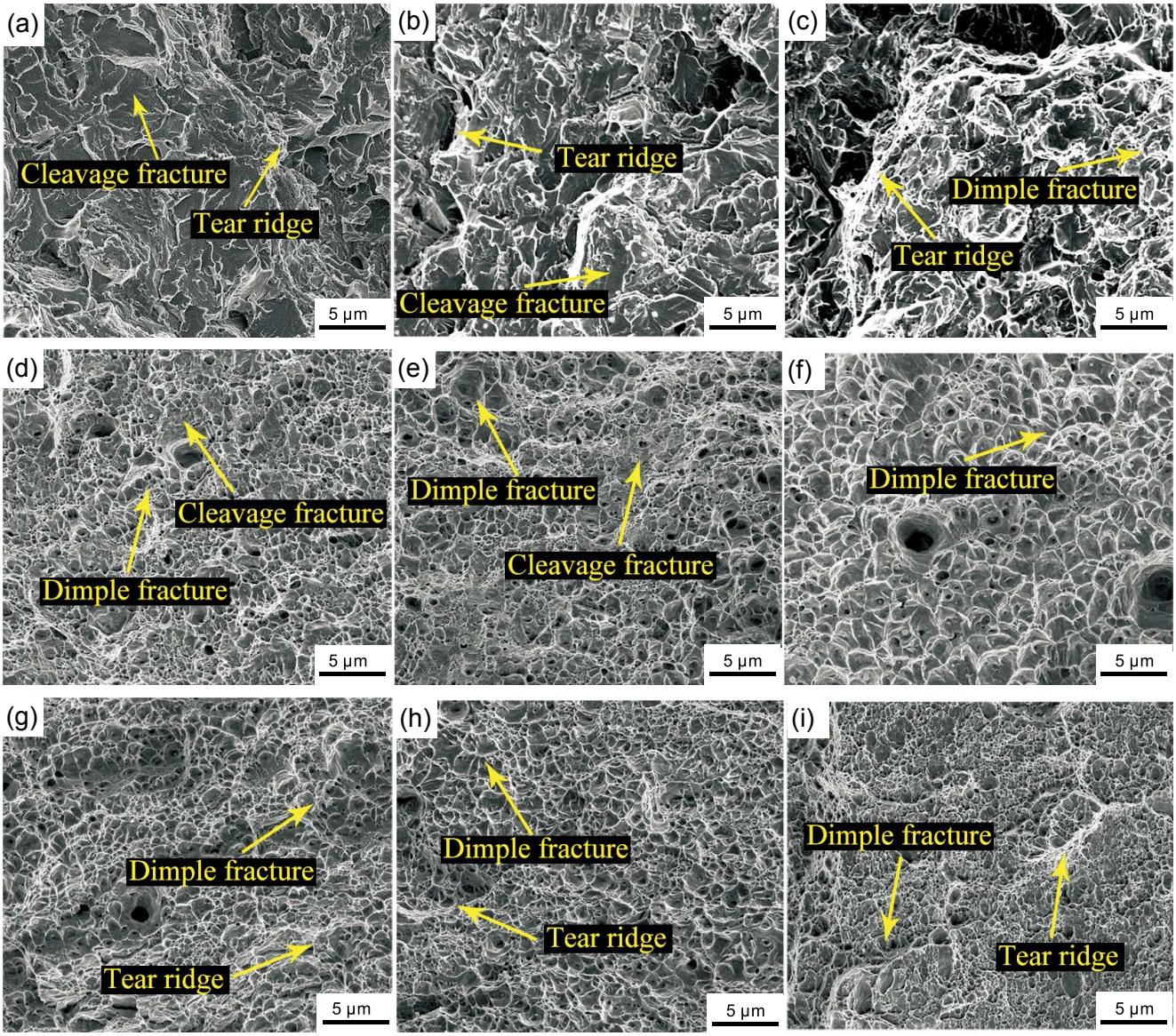

Fig. 13: SEM images of tensile-fracture morphologies of DLD 12CrNi2 samples. (a) Top, (b) middle, and (c) bottom layers in Sample 1; (d) top, (e) middle, and (f) bottom layers in Sample 2; (g) top, (h) middle, and (i) bottom layers in Sample 3

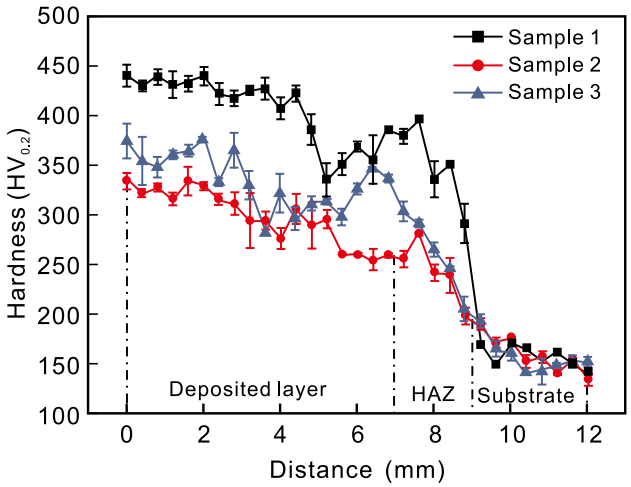

Fig. 14: Variation in hardness along deposited layers in DLD samples

composed of W, and the deformation resistance of W is higher than that of M_L and F_B. Therefore, the hardness of the S1 sample is higher than that of the S2 and S3 samples. Compared with the top region of the S1 sample, the deformation resistance of the bottom region of the S1 sample is decreased, resulting in a lower hardness of the bottom deposition layer. Due to the great amount of M_L inside the S3 sample, the S3 sample has a higher resistance to deformation. Therefore, the average hardness of the S3 sample is higher than that of the S2 sample.

4 Conclusions

This study explored three scanning strategies to understand how the microstructural evolution and mechanical properties of the deposited 12CrNi2 steel were impacted by the idle time and laser power between layers. The following conclusions

can be obtained:

(1) Compared with the top region of the 12CrNi2 deposited sample, the bottom region is tempered by the subsequent depositing layers, resulting in more M-A islands in the structure.

(2) Compared with the continuous deposition strategy, the scanning strategy with idle time between layers and decreasing laser power layer by layer can reduce the inter-layer temperature and the maximum temperature of the molten pool, so that the deposition sample is subjected to a weaker tempering effect and maintains a higher cooling rate.

(3) The ratio of lath martensite in 12CrNi2 deposited sample can be increased by the scanning strategy with idle time between layers and decreasing laser power layer by layer, so as to improve the yield strength of the deposited sample. Under this scanning strategy, the tensile strength and elongation of 12CrNi2 sample are in the range of 873–1022 MPa and 16.2%–18.9%, respectively.

(4) The lath shape morphology in the top region of the samples is more obvious, while the lath shape in the bottom region of the samples is weakened, and more M-A islands or granular microstructure are found.

(5) Compared with the top region of the samples, the elongation at the bottom region of the samples is greater, and the ductile fracture characteristics are more obvious. The tensile strength at the top region of the samples is greater than that at the bottom region of the samples, and the cleavage fracture characteristics on the fracture surface of the top region are more obvious.

Acknowledgement

This research work was financially supported by the National Key Technologies Research and Development Program of China (Grant No. 2016YFB1100200).

References

[1] Chen S, Wang R, Chen X, et al. Effect of Ce element on microstructure and properties of 12CrNi2Ce alloy steel prepared by laser direct metal deposition. Journal of Laser Applications, 2018, 30: 032020.

[2] Shakerin S, Hadadzadeh A, Amirkhiz B S, et al. Additive manufacturing of maraging steel-H13 bimetals using laser powder bed fusion technique. Additive Manufacturing, 2019, 29: 1–15.

[3] Guo P, Zou B, Huang C, et al. Study on microstructure, mechanical properties and machinability of efficiently additive manufactured AISI316L stainless steel by high-power direct laser deposition. Journal of Materials Processing Technology, 2017, 240: 12–22.

[4] Li N, Huang S, Zhang G D, et al. Progress in additive manufacturing on new materials: A review. Journal of Materials Science and Technology, 2019, 35: 242–269.

[5] Sun G F, Shen X T, Wang Z D, et al. Laser metal deposition as repair technology for 316L stainless steel: Influence of feeding powder compositions on microstructure and mechanical properties. Optics and Laser Technology, 2019, 109: 71–83.

[6] Cui R, Cheng Y, Meng X, et al. Microstructure and properties of heat treated 1Cr17Ni4MoB steel fabricated by laser melting deposition. Optics and Laser Technology, 2018, 108: 59–68.

[7] Zhou Y, Chen S Y, Chen X T, et al. The evolution of bainite and mechanical properties of direct laser deposition 12CrNi2 alloy steel at different laser power. Materials Science and Engineering: A, 2018, 742: 150–161.

[8] Guan T T, Chen S Y, Chen X T, et al. Effect of laser incident energy on microstructures and mechanical properties of 12CrNi2Y alloy steel by direct laser deposition. Journal of Materials Science and Technology, 2019, 35(2): 395–402.

[9] Dong Z, Kang H, Xie Y, et al. Effect of powder oxygen content on microstructure and mechanical properties of a laser additively-manufactured 12CrNi2 alloy steel. Materials Letters, 2019, 236: 214–217.

[10] Zuo P, Chen S, Wei M, et al. Thermal behavior and grain evolution of 24CrNiMoY alloy steel prepared by pre-laid laser cladding technology. Optics and Laser Technology, 2019, 119: 105613.

[11] Zheng B, Zhou Y, Smugeresky J E, et al. Thermal behavior and microstructural evolution during laser deposition with laser-engineered net shaping: Part I. Numerical calculations. Metallurgical and Materials Transactions: A, 2008, 39: 2228–2236.

[12] Costa L, Vilar R, Reti T, et al. Rapid tooling by laser powder deposition: Process simulation using finite element analysis. Acta Materialia, 2005, 53: 3987–3999.

[13] Manvatkar V D, Gokhale A A, Reddy G J, et al. Estimation of melt pool dimensions, thermal cycle, and hardness distribution in the laser-engineered net shaping process of austenitic stainless steel. Metallurgical and Materials Transactions: A, 2011, 42: 4080–4087.

[14] Yadollahi A, Shamsaei N, Thompson S M, et al. Effects of process time interval and heat treatment on the mechanical and microstructural properties of direct laser deposited 316L stainless steel. Materials Science and Engineering: A, 2015, 644: 171–183.

[15] Kang X, Dong S, Men P, et al. Microstructure evolution and gradient performance of 24CrNiMo steel prepared via laser melting deposition. Materials Science and Engineering, 2020, 777: 1–12.

[16] Kang X, Dong S, Wang H, et al. Effect of Thermal Cycle on Microstructure Evolution and Mechanical Properties of Selective Laser Melted Low-Alloy Steel. Materials, 2019, 12(21): 1–15.

[17] Karmakar P, Gopinath M, Nath A K. Effect of tempering on laser remelted AISI H13 tool steel. Surface and Coatings Technology, 2019, 361: 136–149.